PNAS RESEARCH ARTICLE | CELL BIOLOGY

Mitochondrial outer membrane protein FUNDC2 promotes ferroptosis and contributes to doxorubicin-induced cardiomyopathy

Na Ta[a,b,c], Chuanren Qu[a,b,c], Hao Wu[d], Di Zhang[a,e], Tiantian Sun[e], Yanjun Li[e], Jun Wang[a,c], Xiaohui Wang[a,c], Tieshan Tang[a,b,c], Quan Chen[e,1], and Lei Liu[a,b,c,1]

Edited by Douglas Wallace, University of Pennsylvania, Philadelphia, PA; received September 22, 2021; accepted June 7, 2022

Ferroptosis is an iron-dependent programmed necrosis characterized by glutathione (GSH) depletion and lipid peroxidation (LPO). Armed with both the pro- and antiferroptosis machineries, mitochondria play a central role in ferroptosis. However, how mitochondria sense the stress to activate ferroptosis under (patho-)physiological settings remains incompletely understood. Here, we show that FUN14 domain–containing 2, also known as HCBP6 (FUNDC2), a highly conserved and ubiquitously expressed mitochondrial outer membrane protein, regulates ferroptosis and contributes to doxorubicin (DOX)–induced cardiomyopathy. We showed that knockout of FUNDC2 protected mice from DOX-induced cardiac injury by preventing ferroptosis. Mechanistic studies reveal that FUNDC2 interacts with SLC25A11, the mitochondrial glutathione transporter, to regulate mitoGSH levels. Specifically, knockdown of SLC25A11 in FUNDC2-knockout (KO) cells reduced mitoGSH and augmented erasin-induced ferroptosis. FUNDC2 also affected the stability of both SLC25A11 and glutathione peroxidase 4 (GPX4), key regulators for ferroptosis. Our results demonstrate that FUNDC2 modulates ferroptotic stress via regulating mitoGSH and further support a therapeutic strategy of cardioprotection by preventing mitoGSH depletion and ferroptosis.

mitochondria | FUNDC2 | ferroptosis | SLC25A11 | mitoGSH

Ferroptosis is an iron-dependent programmed cell death with the characteristics of glutathione depletion and lipid peroxidation (LPO) (1). Great strides have been made over the past decade to characterize the molecular pathways involved in ferroptosis (1–9). Small molecule compounds such as erastin and RSL3 can inhibit the import of cysteine or target the phospholipid peroxidase GPX4, respectively, leading to the collapse of cellular redox homeostasis and ferroptosis (1, 2). These studies confirm glutathione (GSH) metabolism as the key machinery in the defense against lipid peroxidation and ferroptosis, and inactivation of such defense systems causes ferroptosis. Numerous other biological processes, including polyunsaturated fatty acid metabolism, NADPH, and coenzyme Q10 were found to suppress or drive ferroptosis via regulating cellular redox homeodynamics and lipid peroxidation (4, 10–12). Accumulating evidence has shown that ferroptosis is associated with cardiomyopathy, heart ischemia–reperfusion injury, and numerous other diseases (13–17). These studies have raised the possibility of exploiting and defending against ferroptotic vulnerability under different pathophysiological conditions, including cardiovascular diseases.

Since the discovery of ferroptosis, the mitochondrion has been suggested to play a central role. Early electron microscopic (EM) analysis revealed that ferroptotic cells typically contain shrunken mitochondria with increased inner membrane density (1). Mitochondria utilize oxygen during oxidative phosphorylation (OXPHOS) for adenosine triphosphate (ATP) production. They are also the center for cellular lipid metabolism, iron metabolism, and reactive oxygen species (ROS) production (18), rendering them particularly susceptible to lipid peroxidation, a hallmark of ferroptosis. During evolution, mitochondria have therefore evolved defense machineries against ferroptosis. These include the mitochondrial form of GPX4 (mitoGPX4), which detoxifies peroxidized lipids, and mitochondrial ferritin, which chelates and stores liable iron to prevent it from damaging organelles (3, 13). Recent work from Gan and coworkers showed that mitochondrial dihydroorotate dehydrogenase (DHODH) works together with mitoGPX4 in mitochondria to detoxify lipid peroxides and defends against ferroptosis (3). The specific role of mitochondria during the progression of ferroptosis remains poorly understood.

Mitochondria house sophisticated redox-sensitive components and are dependent on redox balance to maintain normal functions (19, 20). Redox imbalance, including excessive depletion or oxidation of the mitochondrial GSH (mitoGSH) pool, is associated

Significance

Mitochondria play a vital role in the progression of ferroptosis, an iron-dependent programmed necrosis that is associated with a series of diseases, including cardiomyopathy and heart ischemia–reperfusion injury. However, the molecular mechanism underpinning the link between mitochondria and ferroptosis remains incompletely understood. Here, we found that mitochondrial outer membrane protein FUN14 domain–containing 2, also known as HCBP6 (FUNDC2), could interact with and destabilize SLC25A11 to affect mitochondrial glutathione (mitoGSH) levels, and thus to regulate ferroptosis. This FUNDC2–SLC25A11 axis serves as a pathway for the regulation of ferroptosis through mitochondria and provides insights into the therapeutic interventions of ferroptosis-related diseases.

Author contributions: N.T., Q.C., and L.L. designed research; N.T., C.Q., H.W., D.Z., T.S., and Y.L. performed research; J.W., X.W., and T.T. contributed new reagents/analytic tools; N.T., Q.C., and L.L. analyzed data; and N.T., Q.C., and L.L. wrote the paper.

The authors declare no competing interest.

This article is a PNAS Direct Submission.

See online for related content such as Commentaries.

[1]To whom correspondence may be addressed. Email: chenq@nankai.edu.cn or liulei@ioz.ac.cn.

This article contains supporting information online at http://www.pnas.org/lookup/suppl/doi:10.1073/pnas.2117396119/-/DCSupplemental.

Published August 29, 2022.

with several pathophysiological conditions (21). Mitochondria contain 10 to 15% of the total cellular GSH, although they do not produce GSH (22, 23). At physiological pH, GSH is negatively charged and thus impermeable to mitochondria. To enter the mitochondrial matrix, GSH solely relies on the mitochondrial carrier proteins such as SLC25A11 (24–26). GSH protects against ROS, electrophiles, xenobiotics, and protein thiol oxidation, and it is critical for mitochondrial bioenergetics, including the tricarboxylic acid (TCA) cycle, fatty acid metabolism, OXPHOS and mitochondrial integrity (27). MitoGSH also plays an important role in iron homeostasis and iron–sulfur cluster assembly inside mitochondria (28, 29). It also serves as a cofactor for GPX4 to reduce lipid peroxidation (30, 31), and mitochondrially localized GPX4 was found to play a key role in the protection from acute injury induced–cardiomyopathy (13). These studies point toward a potential role of mitoGSH in ferroptosis.

FUNDC2 (FUN14 domain–containing 2, also known as HCBP6) (32, 33) is a conserved mitochondrial outer membrane protein with two transmembrane domains. Previously, we reported that FUNDC2 regulates mitochondrial-dependent death in platelets in response to hypoxia (34). In an effort to understand the molecular functions of FUNDC2, we noticed that the cardiac function remained unaffected when FUNDC2 was deficient, although FUNDC2 is highly expressed in the heart, leading us to investigate the role of FUNDC2 in cardiac injury. Here, we found that FUNDC2 interacts with SLC25A11 to regulate mitoGSH and ferroptosis. This previously unknown FUNDC2–SLC25A11 axis is critical for ferroptosis regulation and plays a pivotal role in cardioprotection in response to doxorubicin (DOX)-induced heart injury.

Results

Knockout of FUNDC2 Ameliorates DOX-Induced Cardiomyopathy. We first screened FUNDC2 protein levels in major organs by Western blotting analysis and found that FUNDC2 is highly expressed in the heart, indicating its potential functions there (Fig. 1*A*). Despite the complete loss of FUNDC2 protein (Fig. 1*B*), the FUNDC2-knockout (KO) offspring were born at Mendelian ratio and appeared grossly normal. At baseline, adult FUNDC2-KO mice have normal body weight and normal heart functions (Fig. 1*C*–*G*, control groups). We were interested to see whether FUNDC2 plays a role in response to cardiac injury. Doxorubicin (DOX) is a widely used clinical anticancer medicine, with known side effects of cardiotoxicity. By injecting a single dose of 10 mg/kg DOX (saline as control) to both wild-type (WT) and FUNDC2-KO mice, we found that loss of body weight and heart weight was significantly less in FUNDC2-KO compared to the WT mice (Fig. 1*C*). Transthoracic echocardiography was used to evaluate the cardiac functions by measuring the left ventricular ejection fraction (LVEF) and left ventricular fractional shortening (LVFS), indicators of left ventricular systolic function (Fig. 1*D*). There was no significant difference in LVEF and LVFS in the WT and FUNDC2-KO mice treated with saline (control), whereas the cardiac functions were much better preserved after DOX-treatment in FUNDC2-KO mice compared to the WT controls (Fig. 1*E*). In agreement with this, the mRNA levels of heart failure biomarkers (14, 15), i.e., *Anp* (atrial natriuretic peptide), *Bnp* (brain natriuretic peptide), and *Myh7* (myosin-7), were all significantly up-regulated by DOX in the WT hearts, but not in the FUNDC2-KO hearts (Fig. 1*F*). Of note, there was no difference in saline-treated groups (Fig. 1*F*). Masson's Trichrome staining indicated that knockout of FUNDC2 prevents DOX-induced cardiac fibrosis (Fig. 1*G*). Collectively, these results suggest that the loss of function of FUNDC2 protects mice from DOX-induced cardiomyopathy.

Knockout of FUNDC2 Ameliorates DOX-Induced Ferroptosis. Recent reports indicate that ferroptosis plays an important role in DOX-induced cardiotoxicity (13, 15). We speculated that FUNDC2 may modulate ferroptosis to affect DOX-induced cardiotoxicity. Therefore, we first checked whether ferrostatin-1 (Fer-1), a widely used ferroptosis inhibitor, can ameliorate DOX-induced cardiomyopathy. Consistent with previous reports, Fer-1 pretreatment strongly protected against cardiac damage in both WT and FUNDC2-KO mice (Fig. 1*C*–*G*). To further ascertain the role of FUNDC2 with DOX-induced ferroptosis, we analyzed the expression of *Ptgs2* mRNA, a biochemical hallmark for ferroptosis. As expected, DOX induced a significant nearly threefold up-regulation of cardiac *Ptgs2* mRNA in the WT mice, which was abolished by Fer-1 pretreatment (Fig. 2*A*). However, no change in *Ptgs2* mRNA expression was observed in the KO mice (Fig. 2*A*). In addition, knockout of FUNDC2 failed to protect staurosporine (STS)-induced apoptosis, TNF-α/SM-164/Z-VAD-FMK (T/S/V) induced necroptosis, starvation-induced autophagy, and H_2O_2-induced necrosis in mouse embryo fibroblast (MEF) cells (*SI Appendix*, Fig. S1*A*–*G*) compared to WT cells, indicating a ferroptosis-specific role of FUNDC2.

We further checked the level of 4-hydroxynonenal (4-HNE), a biomarker of lipid peroxidation and a key indicator of ferroptosis in vivo (15, 16, 32). We found that 4-HNE levels were significantly increased in the cardiac tissue of the DOX-treated WT mice, but not in the FUNDC2-KO mice (Fig. 2*B* and *C*). We also analyzed the levels of malondialdehyde (MDA), a product of lipid peroxidation (15, 32, 33), and found its up-regulation could only be detected in WT mice, but not in the FUNDC2-KO mice (Fig. 2*D*, *Left*). Previous studies have suggested that the mitochondria are responsible for the increase of MDA in response to DOX (13, 15). We then isolated the subcellular fractions of cardiac tissues and found that DOX treatment enhanced the MDA levels in mitochondria, but not in the cytoplasm (Fig. 2*D*, *Middle*, *Right*). Notably, such MDA increase was only observed in the WT but not the FUNDC2-KO mice (Fig. 2*D*, *Middle*, *Right*). Our results are consistent with the observation that DOX treatment enhanced lipid peroxidation specifically in the mitochondria (13, 15). Conversely, FUNDC2 deficiency can prevent the increase of DOX-induced lipid peroxidation. We further examined mitochondrial morphology using EM and found that the mitochondria in DOX-treated hearts were ruptured, with distorted cristae and reduced cristae density. In contrast, FUNDC2 deficiency largely prevented such mitochondrial damage (Fig. 2*E*). Finally, Fer-1 strongly prevents the DOX-induced mitochondrial deformation, indicating a DOX–mitochondria–ferropotosis signaling axis (Fig. 2*E*).

FUNDC2-KO Inhibits Erastin-Induced Cell Death. GSH metabolism lies at the center of redox metabolism and ferroptosis (2). We measured the total GSH/glutathione disulfide (GSSG) ratio and GSH levels in cardiac tissue and found that the GSH/GSSG ratio and GSH levels in FUNDC2-KO myocardium were much higher than those in the WT groups (Fig. 3*A* and *SI Appendix*, Fig. S2*A*). As FUNDC2 is a mitochondrial protein, we sought to determine whether FUNDC2 regulates mitochondrial GSH. Indeed, the mitochondrial GSH/GSSG ratio and GSH levels in the FUNDC2-KO hearts were higher compared to those in the WT group (Fig. 3*A* and *SI Appendix*, Fig. S2*A*). Strikingly, both total and the mitochondrial GSH/GSSG ratio and GSH levels

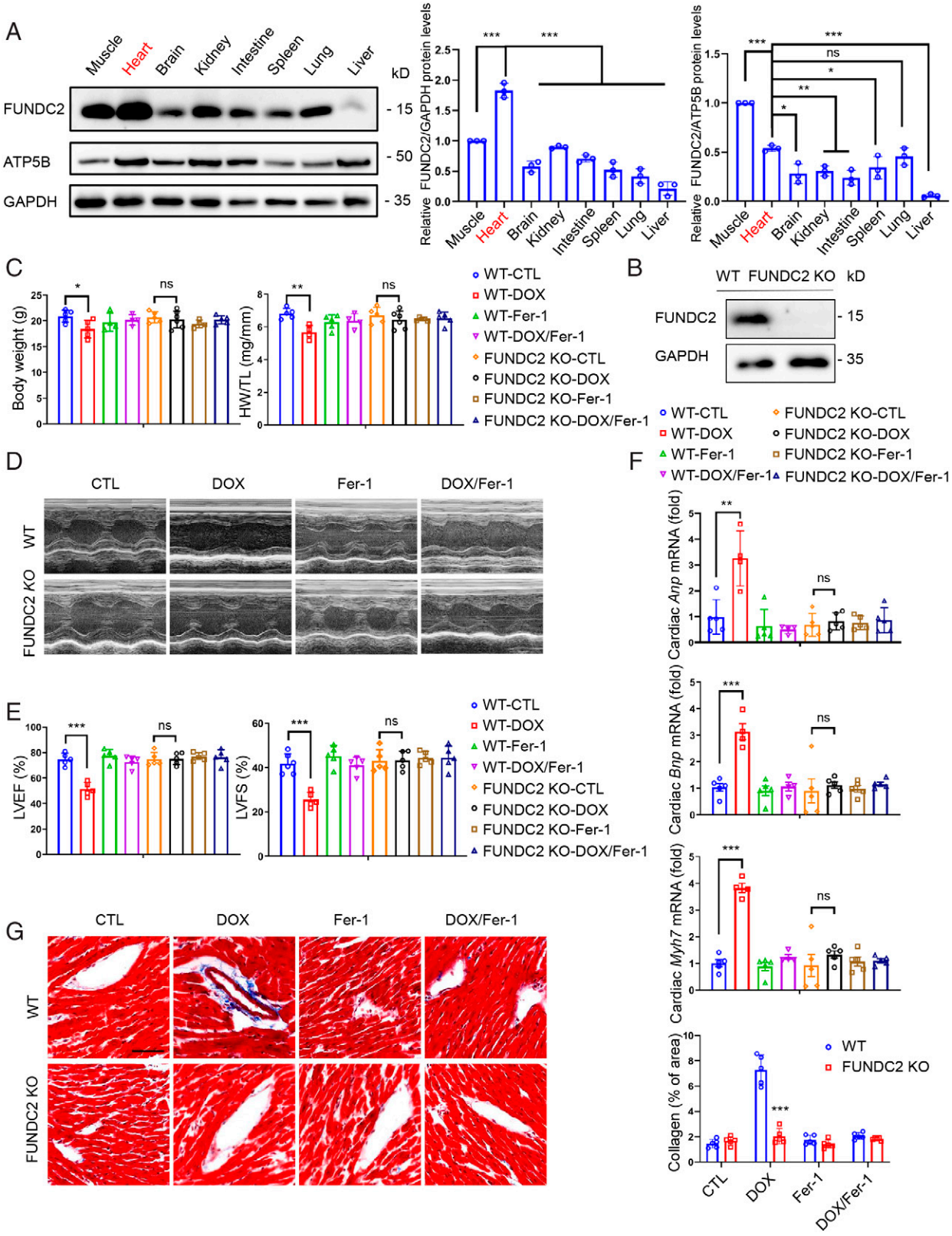

Fig. 1. Knockout of FUNDC2 ameliorates doxorubicin-induced cardiomyopathy. (*A*) Relative expression levels of FUNDC2 in different tissues of the male mouse were analyzed by Western blotting (*Left*) and quantified with GAPDH (*Middle*) or mitochondrial protein ATP5B (*Right*) as the internal control ($n = 3$ mice). (*B*) Immunoblot of FUNDC2 and GAPDH in heart tissue lysates from WT and FUNDC2-KO male mice. (*C–G*) Body weight (*Left*) and heart weight (HW)/tibial length (TL) ratio were measured in WT and FUNDC2-KO mice subjected to DOX or saline (control) in the presence or absence of ferrostatin-1 (Fer-1) at day 4 ($n = 4$ to 5 mice) (*C*). For each group subject, the echocardiogram was performed (*D*); LVEF (*Left*) and LVFS (*Right*) were measured ($n = 4$ to 5 mice) (*E*); the relative mRNA levels of *Anp*, *Bnp*, and *Myh7*, cardiac hypertrophy biomarkers, were analyzed by qPCR ($n = 4$ to 5 mice) (*F*); and the collagen fibrosis in myocardium were visualized by Masson's Trichrome staining (*Left*) and quantified by collagen volume fraction (%, collagen fibrosis per total myocardium) (*Right*). (Scale bar, 50 μm.) ($n = 4$ to 5 mice) (*G*). Statistical significance was calculated by Student *t* test (*G*) and one-way ANOVA (*A*, *C*, *E*, and *F*);*$P < 0.05$, **$P < 0.01$, ***$P < 0.001$ and ns indicates no significance.

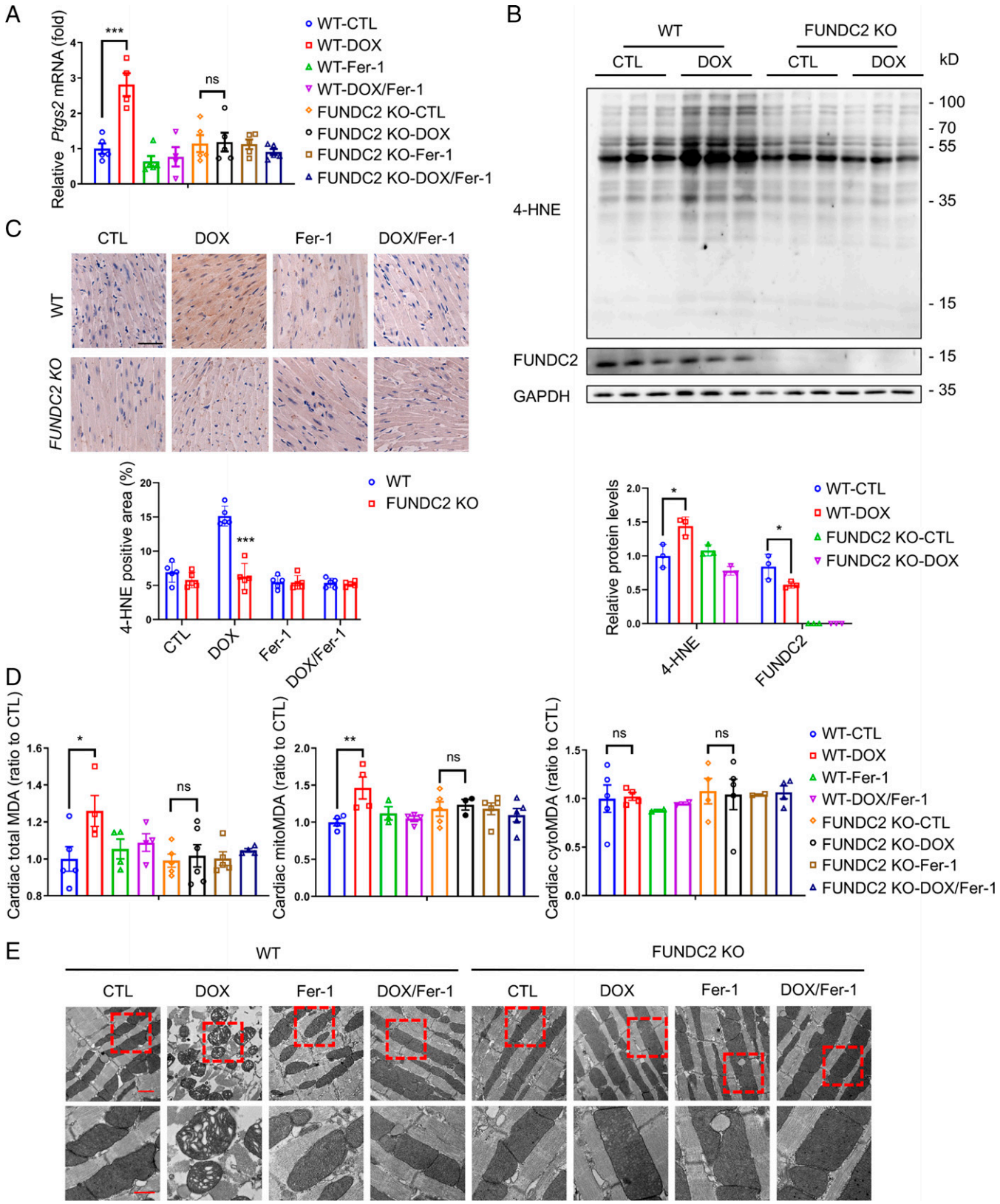

Fig. 2. Knockout of FUNDC2 mitigates doxorubicin-induced ferroptosis. (*A*–*E*) For the mice both WT and FUNDC2-KO subjected to DOX or saline (control) treatment in the presence or absence of Fer-1 at day 4, the relative levels of *Ptgs2* mRNA in myocardium were measured by qPCR (n = 4 to 5 mice) (*A*), and their expression levels of 4-HNE in hearts were analyzed and quantified relative to GAPDH by immunoblot analysis (n = 3 mice) (*B*). The cardiac tissues of mice from each group were stained with anti–4-HNE (*Top*) and quantitative analysis was performed (*Bottom*). (Scale bars, 50 μm [*Top*].) (n = 4 to 5 mice) (*C*). MDA levels in the whole (*Left*), the cytosolic fraction (*Middle*), and the mitochondrial fraction (*Right*) (n = 4 to 5 mice) (*D*) of the myocardium tested were measured. Representative EM images of cardiac tissues (*E*) were obtained. (Scale bars, 1 μm [*Top*] and 500 nm [*Bottom*].) Statistical significance was calculated by Student's t test (*C*) and one-way ANOVA (*A*, *B*, and *D*); $^{*}P < 0.05$, $^{**}P < 0.01$, $^{***}P < 0.001$ and ns indicates no significance.

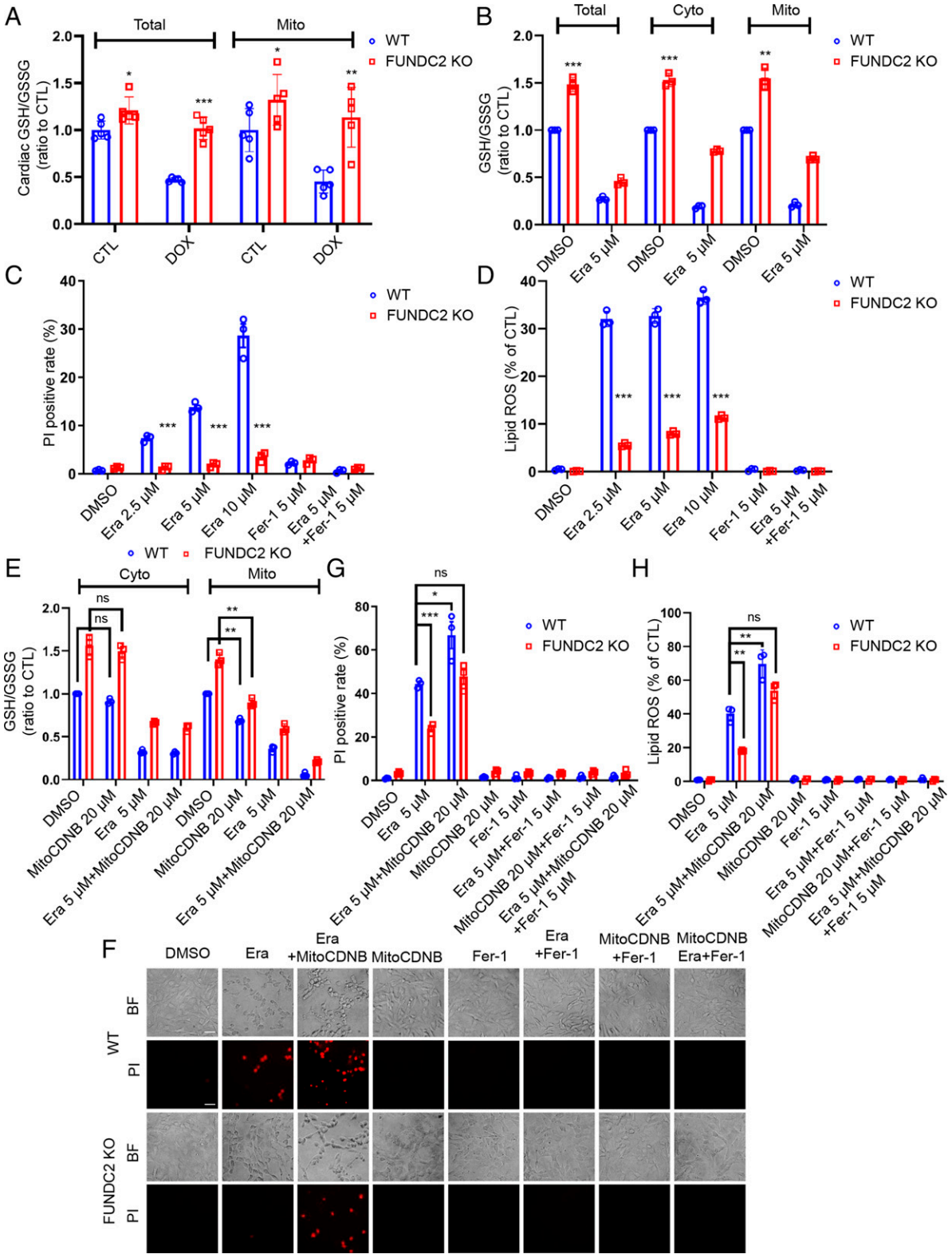

Fig. 3. FUNDC2-KO inhibits but mitoGSH depletion increases erastin-induced cell death. (*A*) The cardiac glutathione (GSH)/GSSG ratio and the cardiac mitochondrial (mito) GSH/GSSG ratio of each mouse were measured in WT and FUNDC2-KO mice subjected to DOX or saline (control [CTL]). (*B–D*) Cellular, cytosolic (Cyto), and mitochondrial (Mito) GSH/GSSG ratio were determined in WT and FUNDC2-KO MEF cells after being treated with 5 μM erastin or dimethyl sulfoxide (DMSO) for 3 h (*B*). These two types of cells were treated with 2.5 μM, 5 μM, and 10 μM erastin or DMSO for 6 h or 4 h in the presence or absence of 5 μM Fer-1; after that, the cell death of each group was determined by PI staining coupled with flow cytometry (6 h) (*C*); and the lipid ROS level of each group was analyzed by C11-BODIPY staining coupled with flow cytometry (4 h) (*D*). (*E–H*) Cyto and Mito GSH/GSSG ratio were determined in WT and FUNDC2-KO MEF cells after being incubated with 5 μM erastin or DMSO for 3 h with or without the pretreatment of 20 μM MitoCDNB (*E*). In addition, both cell types pretreated with 20 μM MitoCDNB or not were incubated with 5 μM erastin or DMSO for 6 h or 4 h with the presence or absence of 5 μM Fer-1. Then cell death was visualized by PI staining coupled with microscopy in both the brightfield (BF) (*Top*) and fluorescent (*Bottom*) modes (Scale bar, 20 μm.) (*F*) at the same position and further analyzed by PI staining coupled with flow cytometry (6 h) (*G*); and the lipid ROS level was determined by C11-BODIPY staining coupled with flow cytometry (4 h) (*H*). Data from three independent experiments and statistical significance was calculated by Student's *t* test; $^{*}P < 0.05$, $^{**}P < 0.01$, $^{***}P < 0.001$ and ns indicates no significance.

were reduced to ~50% by DOX treatment in WT hearts but were preserved in the KO hearts (Fig. 3*A* and *SI Appendix*, Fig. S2*A*). These data demonstrated that high GSH levels, particularly mitoGSH, appear to be cardioprotective in the context of DOX-induced cardiotoxicity.

To further understand the molecular mechanism of how FUNDC2 regulates mitoGSH, we performed in vitro studies with WT and FUNDC2-KO MEF cells (*SI Appendix*, Fig. S2*B*). Consistent with in vivo results, mitochondrial and the cytosolic GSH/GSSG ratio and GSH (cytoGSH) levels and in FUNDC2-KO MEF cells were much higher than those in the WT MEF cells (Fig. 3*B* and *SI Appendix*, Fig. S2*C*). Erastin treatment reduced the GSH/GSSG ratio and GSH levels from both WT and FUNDC2-KO MEF cells, but the GSH/GSSG ratio and GSH levels remained higher in FUNDC2-KO MEF cells compared to those in WT MEF cells under all conditions (Fig. 3*B* and *SI Appendix*, Fig. S2*C*). The GSH levels were correlated with cell death in response to erastin (Fig. 3*C* and *SI Appendix*, Fig. S2*D* and *E*), indicating a functional importance of GSH in ferropotosis. Lipid ROS accumulation was measured by flow cytometry using C11-BODIPY, a fluorescent probe of lipid peroxidation, which demonstrated that FUNDC2 deficiency prevented the erastin-induced lipid ROS accumulation (Fig. 3*D*). Further, the erastin-induced lipid ROS accumulation was evident on mitochondria (*SI Appendix*, Fig. S2*F*) and FUNDC2 deficiency prevented most erastin-induced mitochondrial damage (*SI Appendix*, Fig. S2*G*). In sharp contrast with the WT cells, erastin-induced *Ptgs2* mRNA expression was largely abolished in FUNDC2-KO MEF cells (*SI Appendix*, Fig. S2*H*). In addition, we performed in vitro studies with WT and FUNDC2-knockdown (KD) H9c2 cells, a rat cardiomyocyte line. Consistent with the in vivo results, mitochondrial GSH levels and the GSH/GSSG ratio in FUNDC2-KD H9c2 cells were much higher than in the WT H9c2 cells (*SI Appendix*, Fig. S3*A–C*). FUNDC2 KD also prevented DOX-induced cell death, lipid peroxidation, and mitochondria damage in H9c2 cells (*SI Appendix*, Figs. S3*D* and *E* and S4*A–C*).

DOX-induced ferroptosis was also confirmed in MEF cells. Consistently, FUNDC2 deficiency prevented DOX-induced cell death, lipid peroxidation, and mitochondria damage (*SI Appendix*, Figs. S4*D–F* and S5*A–E*), and this effect was rescued by reintroducing FUNDC2 into FUNDC2-KO MEF cells (*SI Appendix*, Fig. S5*A–E*). Conversely, overexpression of FUNDC2 enhanced DOX-induced cell death and lipid peroxidation (*SI Appendix*, Fig. S5*F–J*).

We also investigated the role of FUNDC2 in the context of other ferroptosis inducers, including sulfasalazine (SASP), L-buthionine-sulfoximine (BSO), and RSL3 (2). SASP and BSO reduce the GSH levels by direct inhibition of cysteine/glutamate antiporter system Xc^- activity and GSH biosynthesis, respectively, while RSL3 induces ferroptosis by inhibiting GPX4. As shown in *SI Appendix*, Fig. S6*A–L*, FUNDC2 deficiency inhibited SASP/BSO/RSL3-induced cell death and lipid ROS accumulation. Taken together, these results indicated FUNDC2 mediates ferroptosis, likely through modulating mitochondrial GSH.

To further confirm that FUNDC2 promotes ferroptosis via mitoGSH, we treated MEF cells with MitoCDNB, a specific mitochondrial GSH depletory chemical (27), to selectively deplete the mitochondrial GSH pool. Pretreatment with MitoCDNB reduced the mitochondrial GSH/GSSG ratio and GSH level, which was further reduced after erastin treatment (Fig. 3*E* and *SI Appendix*, Fig. S2*I*). MitoCDNB treatment effectively enhanced erastin-induced cell death (Fig. 3*F* and *G*) and lipid ROS accumulation (Fig. 3*H*) in both WT and FUNDC2-KO MEF cells. Together, these results suggest that mitoGSH depletion indeed increases erastin-induced cell death.

FUNDC2–SLC25A11 Axis Modulates Ferroptosis. To gain insight into the molecular mechanism by which FUNDC2 affects mitoGSH levels, we performed tandem affinity purification (TAP) in combination with the mass spectrometry (MS) to identify proteins that may directly interact with FUNDC2. Among the multiple candidates identified, we were intrigued by SLC25A11, a known mitochondrial GSH transporter (24–26) (*SI Appendix*, Fig. S7*A*). SLC25A11 is localized in the mitochondrial inner membrane, serving as a mitochondrial GSH transporter to import GSH into mitochondria. Coimmunoprecipitation (Co-IP) analysis revealed that FUNDC2 specifically interacted with endogenous SLC25A11 protein in HeLa (*SI Appendix*, Fig. S7*B*) and MEF cells (*SI Appendix*, Fig. S7*C*). Although SLC25A10 was also found to be involved in the import of GSH and other TCA substrates (24, 35, FUNDC2 did not interact with SLC25A10 (*SI Appendix*, Fig. S7*D*). Super-resolution microscopy (structure illumination microscopy, SIM) further confirmed the colocalization of FUNDC2 with SLC25A11 in HeLa cells (*SI Appendix*, Fig. S7*E*).

We next sought to investigate whether the interaction between FUNDC2 and SLC25A11 is of functional consequence in ferroptosis. Using an shRNA approach, we first stably knocked down SLC25A11 in WT and FUNDC2-KO MEF cells (with the scramble shRNA as control) (Fig. 4*A*), and found that SLC25A11 deficiency deceased the mitochondrial GSH/GSSG ratio and GSH levels in both WT and FUNDC2-KO MEF cells without much effect on the cytosolic GSH/GSSG ratio and GSH levels (Fig. 4*B* and *SI Appendix*, Fig. S8*A*). SLC25A11 KD also enhanced erastin-induced ferroptosis regardless of FUNDC2 levels, as evidenced by cell viability, cell death (Fig. 4*C–E*), and lipid ROS accumulation (Fig. 4*F*). These data suggested that SLC25A11 is required for cells to survive against ferroptosis.

We further explored whether the gain of function in SLC25A11 can prevent erastin-induced ferroptosis. We stably transfected the plasmids encoding the vector or Flag-SLC25A11 into WT and FUNDC2-KO MEF cells (Fig. 4*G*), and found that SLC25A11 overexpression increased the mitochondrial GSH/GSSG ratio and GSH levels in both WT and FUNDC2-KO MEF cells, with or without erastin treatment (Fig. 4*H* and *SI Appendix*, Fig. S8*B*). Consequently, SLC25A11 overexpression was sufficient to inhibit the erastin-induced cell death (Fig. 4*I–K*) and lipid ROS accumulation (Fig. 4*L*).

Taken together, these results suggested that SLC25A11 counteracts FUNDC2-dependent ferroptosis.

FUNDC2 Modulates the Stability of SLC25A11. The date above have demonstrated that loss of function in FUNDC2 increases mitoGSH levels via a SLC25A11-dependent mechanism. Here we sought to determine how FUNDC2 regulates SLC25A11. By Western blot assay, we found that FUNDC2-KO could increase the SLC25A11 level and block the erastin-induced reduction of GPX4 and mitochondrial proteins such as TIM23 and TOM20 in MEF cells (Fig. 5*A*). In addition, the SLC25A11 level in cardiac tissue of FUNDC2-KO mice was higher than in WT mice (Fig. 5*B*). No effect was observed with SLC25A10, another SLC25 family member (Fig. 5 A and *B*). Although the mitochondrial proteins and GPX4 were down-regulated in response to DOX in both WT and FUNDC2-KO mice, FUNDC2-KO alleviated the degree of down-regulation (Fig. 5*B*). We then tested whether the interaction between

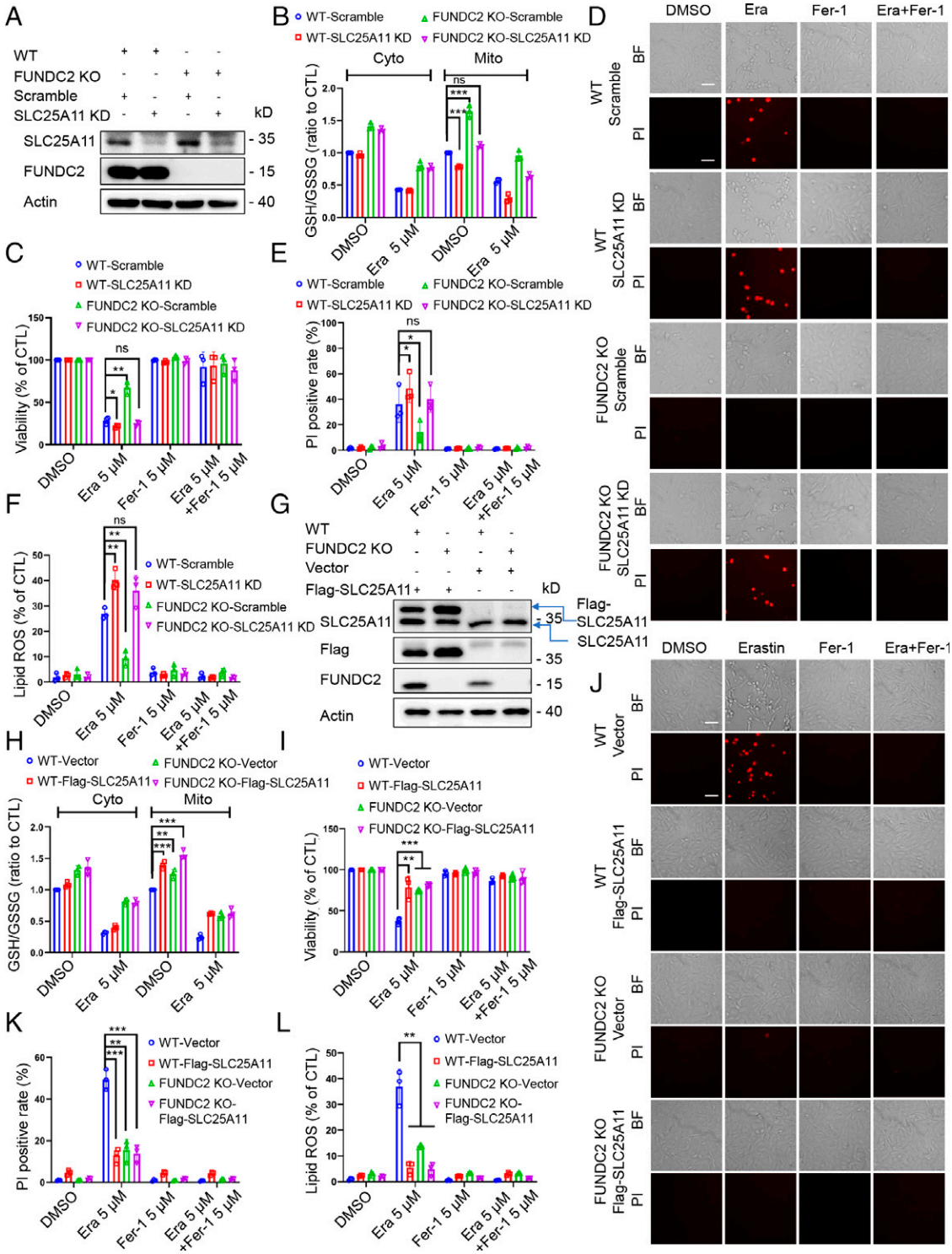

Fig. 4. FUNDC2/SLC25A11 axis modulates ferroptosis. (*A*) Immunoblot analysis of FUNDC2, SLC25A11, and actin in WT, WT/SLC25A11-KD, FUNDC2-KO, and FUNDC2-KO/SLC25A11 KD MEF cells. (*B–F*) Cyto and Mito GSH/GSSG ratio were determined in WT/scramble, WT/SLC25A11-KD, FUNDC2-KO/scramble, and FUNDC2-KO/SLC25A11-KD MEF cells after being treated with 5 μM erastin or DMSO for 3 h (*B*). These four types of cells were treated with 5 μM erastin or DMSO for 6 h or 4 h in the presence or absence of 5 μM Fer-1; then the cell viability was measured by CCK-8 (*C*); the cell death was visualized by PI staining coupled with microscopy in both the brightfield (BF) (*Top*) and fluorescent modes (*Bottom*) (Scale bar, 20 μm.) (*D*) at the same position and further analyzed by PI staining coupled with flow cytometry (6 h) (*E*); and the lipid ROS level was determined by C11-BODIPY staining coupled with flow cytometry (4 h) (*F*). (*G*) Immunoblot analysis of FUNDC2, SLC25A11, and actin in WT/vector, WT/Flag-SLC25A11, FUNDC2-KO/vector, and FUNDC2-KO/Flag-SLC25A11 MEF cells. (*H–L*) Cyto and Mito GSH/GSSG ratio (*H*) were determined in WT/vector and WT/Flag-SLC25A11, as well as FUNDC2-KO/vector and FUNDC2-KO/Flag-SLC25A11 MEF cells after being treated with 5 μM erastin or DMSO for 3 h. These four types of cells were treated with 5 μM erastin or DMSO in the presence or absence of 5 μM Fer-1; then the cell viability was measured by CCK-8 (*I*); the cell death was visualized by PI staining coupled with microscopy in both the brightfield (BF) (*Top*) and fluorescent (*Bottom*) modes (Scale bar, 20 μm.) (*J*) at the same position and further analyzed by PI staining coupled with flow cytometry (6 h) (*K*); and the lipid ROS level was determined by C11-BODIPY staining coupled with flow cytometry (4 h) (*L*). Data from three independent experiments and statistical significance was calculated by one-way ANOVA; $^{*}P < 0.05$, $^{**}P < 0.01$, $^{***}P < 0.001$ and ns indicates no significance.

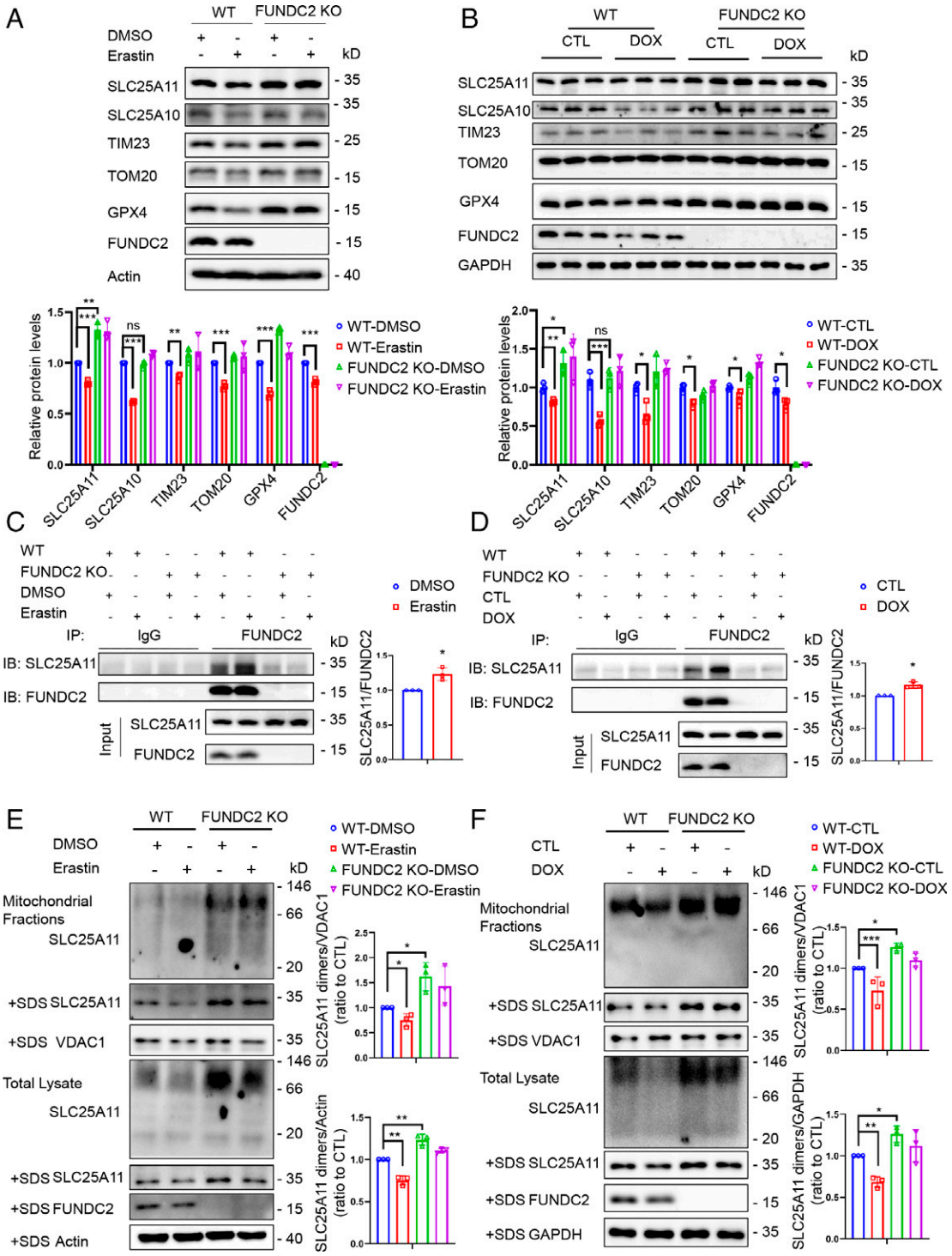

Fig. 5. FUNDC2 regulates SLC25A11 protein. (*A*) Immunoblot analysis of FUNDC2, SLC25A11, SLC25A10, TIM23, TOM20, GPX4, and actin in WT and FUNDC2-KO MEF cells treated with 5 μM erastin or DMSO for 6 h. (*B*) Immunoblot analysis of FUNDC2, SLC25A11, SLC25A10, TIM23, TOM20, GPX4, and GAPDH in myocardium of WT and FUNDC2-KO mice treated with DOX or saline (control) for 4 d ($n = 3$ mice). (*C*) WT and FUNDC2-KO MEF cells treated with 5 μM erastin or DMSO for 3 h were collected for IP with IgG or anti-FUNDC2 antibodies and analyzed with anti-FUNDC2 or SLC25A11 antibodies, respectively. IB, immunoblot. IgG was used as the negative control. (*D*) Cardiac tissues of WT and FUNDC2-KO mice treated with DOX or saline (control) for 3 d were collected for IP with IgG or anti-FUNDC2 antibodies and analyzed with FUNDC2 or SLC25A11 antibodies, respectively. IgG was used as the negative control. (*E*) Dimeric and monomeric forms of SLC25A11 were analyzed in WT and FUNDC2-KO MEF cells and mitochondrial fractions treated with 5 μM erastin or DMSO for 6 h. Mitochondria fractions isolated from the cells and total cellular lysates with the presence or absence of SDS were separated by native PAGE, blotted to NC membranes, and incubated with antibodies against SLC25A11, FUNDC2, VDAC1, and actin. (*F*) Dimeric and monomeric forms of SLC25A11 were analyzed in the cardiac tissues and mitochondrial fractions from WT and FUNDC2-KO mice treated with DOX or saline (control) for 4 d. Mitochondria fractions isolated from cardiac tissues and tissue lysates with the presence or absence of SDS were separated by native-PAGE, blotted to NC membrane, and incubated with antibodies against SLC25A11, FUNDC2, VDAC1, and GAPDH. Data in *A* and *C*–*F* were obtained from three independent experiments. Statistical significance was calculated by Student's *t* test (*C* and *D*) and one-way ANOVA (*A*, *B*, *E*, and *F*); $*P < 0.05$, $**P < 0.01$, $***P < 0.001$ and ns indicates no significance.

FUNDC2 and SLC25A11 is enhanced during ferroptosis. By coimmunoprecipitation assay, we found that erastin treatment reinforced the interaction between FUNDC2 and SLC25A11 (Fig. 5*C*). Similar results were recapitulated in the cardiac tissue in vivo (Fig. 5*D*).

Next, we confirmed whether FUNDC2 regulated the protein stability of SLC25A11. WT and FUNDC2-KO MEF cells were treated with cycloheximide (CHX), an inhibitor of protein synthesis, for different times as indicated in *SI Appendix*, Fig. S9*A*, and the results showed that FUNDC2-KO blocks the CHX-induced reduction of SLC25A11, but not other mitochondrial proteins such as SLC25A10, TIM23, and TOM20 in MEF cells (*SI Appendix*, Fig. S9*A*). However, the SLC25A11 mRNA expression in FUNDC2-KO MEF cells was similar to that in WT MEF cells, with or without erastin treatment (*SI Appendix*, Fig. S9*B*).

As a number of mitochondrial proteins need to be assembled into oligomeric structures to fulfill their functions, we examined the oligomeric state of SLC25A11 by blue native electrophoresis. As shown in Fig. 5*E*, SLC25A11 protein was present in a dimeric form in MEF cells and their mitochondrial fractions lysed with the mild nondenaturing detergent Nonidet P-40, whereas only the monomeric form of SLC25A11 could be observed in lysis with the strong denaturing detergent sodium dodecyl sulfate (SDS). Protein levels of both the dimeric and monomeric forms of SLC25A11 were higher in FUNDC2-KO MEF cells than in WT MEF cells, regardless of erastin treatment (Fig. 5*E*). Similarly, a difference, albeit to a relatively minute extent, could also be observed in the cardiac tissues and their mitochondrial fractions in vivo (Fig. 5*F*). These results suggest that FUNDC2 regulates the stability and dimerization of SLC25A11 to modulate its function.

Discussion

FUNDC2 Regulates Ferroptosis. Previous studies suggest a complex and somewhat controversial role of mitochondria in ferroptosis. Mitochondria are well equipped with both pro- and antiferroptosis machineries (3, 13, 15, 34). The key question is how these machineries are regulated under (patho-)physiological conditions, and how the cytosolic ferroptotic signals are transduced into mitochondria, or vice versa, for ferroptosis. Our surprising finding is that a highly conserved mitochondrial outer membrane protein, FUNDC2, regulates ferroptosis. Knockout of FUNDC2 both in mice and in cultured MEF cells can protect the cells from ferroptosis. Such effects are specific to ferroptosis, as knockout of FUNDC2 fails to block mitochondrial-dependent apoptosis and necroptosis (*SI Appendix*, Fig. S1*A–D*). Knockout of FUNDC2 prevents the doxorubicin-induced mitochondrial deformation in cardiomyocytes and mitochondrial dysfunction in cultured MEF cells. Further studies revealed that knockout of FUNDC2 affects the mitochondrial levels of GSH (Fig. 3*A* and *B* and *SI Appendix*, Fig. S2*A* and *C*), and the stability of mitoGPX4 (*SI Appendix*, Fig. S9*C*), a key regulator for ferroptosis. It appears that FUNDC2 serves as a sentinel at the outer membrane of mitochondria for ferroptotic stress and transduces the signal into the mitochondrial matrix via affecting the transportation of GSH into mitochondria. As such, FUNDC2 may regulate the mitochondrial GSH pool, which is essential for the mitochondrial stress response, the import of mitochondrial proteins, and protein stability and mitochondrial functions. Recent BioID and TurboID analyses have shown that FUNDC2 is localized at mitochondria-associated endoplasmic reticulum (ER) membranes (36), a critical site for mitochondria-ER Ca^{2+} signaling and lipid transfer across membranes (37, 38). It is also possible that FUNDC2 may coordinate the transportation of GSH across the membrane, which may be important for protein folding in ER and mitochondria.

FUNDC2–SLC25A11 Axis Regulates MitoGSH. The major finding of our current study is that FUNDC2 interacts with SLC25A11 to regulate mitoGSH and ferroptosis. Their interaction is increased in DOX-induced cardiomyopathy or under ferroptotic stress in MEF cells (Fig. 5*C* and *D*). Concomitantly, mitoGSH levels were decreased, and mitochondrial ROS and lipid peroxidation are much enhanced. Importantly, knockdown of SLC25A11 in the absence of FUNDC2 reduces mitoGSH and augments ferroptosis in cultured MEF cells. It appears that FUNDC2 is able to modulate the stability of SLC25A11 (*SI Appendix*, Fig. S9*A*) and its dimerization (Fig. 5*E* and *F*), thus regulating mitoGSH. This may be important for fine tuning the import of GSH. As knockout of FUNDC2 improves mitoGSH, we speculate that the function of FUNDC2 is to suppress SLC25A11 activity to some extent, although the precise mechanism remains to be explored. It is also possible that mitochondria have additional systems to maintain the homeostasis of mitoGSH. Previous studies have shown that SLC25A10 in the mitochondrial inner membrane was also involved in the GSH transport into mitochondria (24, 39). However, the silencing of SLC25A10 did not alter mitoGSH levels in FUNDC2-KO cells (*SI Appendix*, Fig. S10*A* and *B*), and the overexpression of SLC25A10 cannot mimic the function SLC25A11 plays to prevent erastin-induced ferroptosis (*SI Appendix*, Fig. S10*C–G*). Also, no interaction between FUNDC2 and SLC25A10 was observed (*SI Appendix*, Fig. S7*D*). Alanine spanning analysis revealed that Q64 residue of FUNDC2 in the intermembrane space of mitochondria is indispensable for the interaction between FUNDC2 and SLC25A11, and such interaction substantially affects the mitochondrial GSH/GSSG ratio (*SI Appendix*, Fig. S11*A–E*). Therefore, we conclude that FUNDC2 regulates mitoGSH by specific interaction with SLC25A11. As a key cellular reductant, GSH lies at the center of redox homeodynamics within mitochondria and plays an essential role in maintaining sulfhydryl-containing proteins in the reduced and active forms and the stability of these proteins (40, 41). Thus, the FUNDC2/SLC25A11 axis monitors the levels of mitoGSH for proper stability and function of GPX4, which is critical for preventing the detrimental effects of ferroptosis inducers on mitochondrial morphology and integrity (1). In supporting this, specific depletion of mitoGSH by mitoCDNB augments erastin-induced ferroptosis. Although the precise details of the interaction between FUNDC2 and SLC25A11 for the import of GSH are not completely understood, our work nonetheless reveals how ferroptotic stress impinges on mitochondria for ferroptosis via affecting mitoGSH, and thus offers mechanisms of molecular regulation of mitoGSH and ferroptosis.

Mitochondria and Ferroptosis in DOX-Induced Heart Injury. DOX is a widely used chemotherapeutic agent that induces progressive, chronic, life-threatening cardiomyopathy, limiting its treatment for malignancies (35, 42). Both cardiomyocyte apoptosis and caspase-independent cell death are attributed to the consequent cell loss, leading to the deterioration of cardiac function (43). DOX accumulates in mitochondria, targets mitochondrial respiration, and inhibits mitochondrial antioxidant mechanisms, leading to aggravated mitochondrial ROS production (44). Moreover, DOX can also induce mitophagy to remove damaged mitochondria (45–49). In fact, we found that the protein levels of FUNDC2 and some mitochondrial proteins such as TIM23,

SLC25A11, and SLC25A10 were also decreased upon DOX treatment, suggesting mitophagy was triggered (Fig. 5*B*). In addition, DOX can interact with iron directly to form a complex that will result in iron cycling between the ferro [Fe (II)] and ferri [Fe (III)] forms for additional ROS production (50). Our work showed that knockout of FUNDC2 in MEF cells and knockdown of FUNDC2 in cardiac cells prevented the DOX-induced mitochondrial superoxide accumulation (*SI Appendix*, Fig. S12*A* and *B*). Recent reports have shown that ferroptosis, along with apoptosis, is the major form of programmed cell death in DOX-induced myocyte death (15). DOX down-regulates GPX4 and induces mitochondrial lipid peroxidation and mitochondrial-dependent ferroptosis, and inhibition of ferroptosis delays or prevents heart injury (13). Our results further extend this finding by showing that mitochondrial FUNDC2 is important for DOX-induced cardiomyopathy. Knockout of FUNDC2 largely prevented DOX-induced cardiomyopathy. Further studies revealed that FUNDC2 regulates mitoGSH and the stability of GPX4 and SLC25A11 required for DOX-induced ferroptosis and heart injury. Our work is in line with most recent reports showing that mitochondrially localized GPX4 suppressed the production of lipid peroxidation and prevented DOX-induced ferroptosis (13). These studies, including ours, highlight a strategy to protect DOX-induced cardiomyopathy by blocking ferroptosis and improving the mitochondrial GSH pool and functions.

Materials and Methods

Reagents and Antibodies. The following reagents were used: Erastin (catalog No. [Cat. No.] S7242, Selleck Chemicals); MitoCDNB (Cat. No. SML2573, Sigma); RSL3 (Cat. No. S8155, Selleck Chemicals); L-buthionine-sulfoximine (Cat. No. B2515, Sigma); sulfasalazine (Cat. No. S1576, Selleck Chemicals); staurosporine (Cat. No. S1421, Selleck Chemicals); Bafilomycin A1 (Cat. No. HY-100558, MedChemExpress); TNF-α (Cat. No. CF09, Novoprotein Scientific); SM-164 (Cat. No. HY-15989, MedChemExpress); necroptosis inhibitor (Cat. No. S8037, Selleck Chemicals); Z-VAD-FMK (Cat. No. S7023, Selleck Chemicals); and cycloheximide (Cat. No. S7418, Selleck Chemicals).

The following antibodies were used: Anti-FUNDC2 antibody was generated by immunizing rabbits with recombinant FUNDC2 protein and purified by affinity chromatography in our laboratory; anti-GPX4 antibody (Cat. No. ab125066, Abcam); anti-SLC25A11 (Cat. No. sc-515593, Santa Cruz); anti-SLC25A11 (Cat. No. 12253-1-AP, Proteintech); anti-SLC25A10 (Cat. No. ARP66277, Aviva Systems Biology); anti-TIM23 antibody (Cat. No. 611223, BD Biosciences); anti-TOM20 antibody (Cat. No. 11802-1-AP, Proteintech); anti-VDAC1 antibody (Cat. No. Ab14734, Abcam); anti-LC3 antibody (Cat. No. PM036, MBL); anti-P62 antibody (Cat. No. PM045, MBL); anti-glyceraldehyde-3-phosphate dehydrogenase (GAPDH) antibody (Cat. No. 60004-1-Ig, Proteintech); anti-Flag antibody (Cat. No. F1804, Merck); and anti-β-actin antibody (Cat. No. A5441, Sigma).

Cell Culture and Establishment of Stable Cell Lines. MEF, HeLa, H9c2, and HEK-293T cells were cultured in Dulbecco's modified Eagle's medium (DMEM) (Gibco) containing 10% fetal bovine serum (FBS) and 1% antibiotics penicillin and streptomycin (P/S) at 37 °C and 5% CO_2 in the incubator. Plasmids were transfected into HeLa and HEK-293T cells using MegaTran 1.0 (Cat. No. TT200003, OriGene). Primers for shRNA target SLC25A11 or scramble shRNA (as a control) were cloned into pSicoR vector. The target sequence in SLC25A11 is 5′-CCTCTTACTCTCAATCTAA-3′. The sequence of the target gene was cloned with pCDH-CMV vector. These vectors were transfected into HEK-293T cells to package viruses. To establish the stable SLC25A11-knockdown cell lines, WT and FUNDC2-KO MEF cells were infected with shRNA expression viruses. To establish stable expression cell lines, WT and FUNDC2-KO MEF cells were infected with target gene expression viruses. These stable cell lines were screened by puromycin (1 mg/mL) for 7 d.

Transient Knockdown of Target Gene. Target gene siRNA and scramble siRNA (as a control) were transfected into MEF and H9c2 cells using RNAiMAX (Cat. No. 13778150, Invitrogen). The target sequence in SLC25A11 (mouse) is 5′-CCTCTTACTCTCAATCTAA-3′; the target sequence in SLC25A10 (mouse) is 5′-ACACTGTGCTCACTTTCAT-3′; and the target sequences in FUNDC2 (rat) are 5′-GACTGGCAGAGACTGGAAA-3′ (sequence 1) and 5′-GCTGTTCGGGCCAGAGTCT-3′ (sequence 2).

Mice and DOX Treatment In Vivo. All protocols were approved by the Institutional Animal Care and Use Committee of the Institute of Zoology accredited by American Association for Accreditation of Laboratory Animal Care International. Adult (6 to 8 wk old) male animals were used in this study. For the generation of FUNDC2-KO mice, the FUNDC2-targeting vector consisting of two genomic fragments, and the neomycin resistance gene (Neo) was used to replace the second coding exon of the FUNDC2 gene following homologous recombination as it was described previously (51). Embryonic stem cell clones (C57BL/6 strain) were used to generate chimeric mice and eventually the FUNDC2-KO mice. For doxorubicin (DOX) treatment, WT and FUNDC2-KO mice were subjected to a single intraperitoneal (i.p.) injection of DOX (Cat. No. S1208, Selleck Chemicals, 10 mg/kg, body weight) or saline (control) at day 4. Mice were given an i.p. injection of ferrostatin-1 (Cat. No. S7243, Selleck Chemicals, 1 mg/kg) or vehicle 1 d before the DOX treatment.

SDS-PAGE and Western Blot Assay. Tissues or cells were collected and lysed in lysis buffer (50 mM Tris-Cl (pH 7.4), 137 mM NaCl, 2 mM ethylene glycol-bis (beta-aminoethyl ether)-N,N,N′,N′-tetraacetic acid (EGTA), 10% glycerol, 1% Nonidet P-40, protease inhibitor mixture). Protein samples were separated by sodium dodecyl sulfate–polyacrylamide gel electrophoresis (SDS-PAGE) gels and then transferred to nitrocellulose membranes. Membranes were blocked by blocking solution (5% skim milk or 5% bovine serum albumin) and then incubated with the primary antibodies against the target proteins, followed by the corresponding horseradish peroxidase (HRP)-conjugated secondary antibodies. Immunoblotted bands were detected using a chemiluminescence (ECL) kit and were analyzed by image J software.

Co-Immunoprecipitation. Tissues or cells were lysed in lysis buffer to obtain tissue or cell lysates as described above. Lysates were treated with the addition of primary antibodies or IgG (as negative control) and then reacted with protein A/G beads overnight at 4 °C under rotary agitation. Afterward, the precipitates were processed for SDS-PAGE and Western blot analysis.

qPCR. Total RNA was extracted from tissues or cells using TRIzol (Invitrogen) and used as the template to synthesize the cDNA by a cDNA Synthesis Kit (Takara). qPCR was carried out using a CFX96 Real-Time System (Bio-Rad) with SYBR Green Master Mix (Tiangen). Relative level of mRNA was calculated after normalization to the actin-β expression level in cells or GAPDH expression level in cardiac tissues. For qPCR, the forward (F) and reverse (R) primer sequences were as follows: *Ptgs2*, 5′-GCGACATACTCAAGCAGGAGCA-3′ (F), 5′-AGTGGTAACCGCT CAGGTGTTG-3′ (R); *Anp*, 5′-TCGTCTTGGCCTTTTGGCT-3′ (F), 5′-TCCAGGTGGTCTAG CAGGTTCT-3′ (R); *Bnp*, 5′-AAGTCCTAGCCAGTCTCCAGA-3′ (F), 5′-GAGCTGTCTCTGG GCCATTTC-3′ (R); *Myh7*, 5′-GCTGAAAGCAGAAAGAGATTATC-3′ (F), 5′-TGGAGTTCTT CTCTTCTGGAG-3′ (R); *SLC25A11*, 5′-CTCGTTACCACTGCTGCTTCCA-3′ (F), 5′-ATAG CGGACGACTTTCAGCAGC-3′ (R); *Gapdh*, 5′-CATCACTGCCACCCAGAAGACTG-3′ (F), 5′-ATGCCAGTGAGCTTCCCGTTCAG-3′ (R); and *Actb*, 5′-CATTGCTGACAGGATGCAGA AGG-3′ (F), 5′-TGCTGGAAGGTGGACAGTGAGG-3′ (R).

Immunofluorescence. HeLa cells transfected with vector and FUNDC2-Myc plasmid were seeded onto coverslips and fixed with 4% paraformaldehyde in phosphate buffered saline (PBS) and then permeabilized with 0.2% Triton X-100. The cells were first incubated with the anti-Myc antibody (Cat. No. MA1980, Thermo Fisher) and anti-SLC25A11(Cat. No. 12253-1-AP, Proteintech), followed by treatment with Alexa488- or Alexa555-conjugated secondary antibodies. The samples were observed with super-resolution microscopy (Delta Vision OMX).

Isolation of Cytosolic and Mitochondrial Fractions from Cells and Cardiac Tissues. Cells or tissues were harvested and resuspended in hypotonic mitochondrial isolation buffer. Cells or tissues were gently homogenized using a Dounce homogenizer and centrifuged at 1,000 × *g* for 10 min at 4 °C to discard the precipitate. The collected supernatant was then centrifuged at 10,000 × *g*

for 10 min at 4 °C to obtain the supernatant containing the cytosolic fractions and the pellet that contained the mitochondria.

Cell Viability Assay. Cell viability was assessed by Cell Counting Kit-8 (Cat. No. C0039, Beyotime). Cells were seeded at 1×10^4 per well in a 96-well plate. After the indicated treatment, the absorbance was measured at 450 nm using a Multi-Plate Reader (Biotek Synergy), based on which the percentage of cell viability was then calculated.

Cell Death Measurement. MEF cells were seeded at 1.5×10^5 per well in a 12-well plate. After the indicated treatment, cell death was determined by propidium iodide (PI) staining (100 ng/mL) coupled with flow cytometry (BD FACS Calibur). PI emission was measured using the FL2 channel. Cell death was visualized by PI staining coupled with microscopy.

Lipid ROS Measurement. The lipid ROS level was analyzed by C11-BODIPY (581/591). The cells were seeded at 1.5×10^5 per well in a 12-well plate. After the indicated treatment, the cells were incubated in 5 μM C11-BODIPY (581/591) (Cat. No. D3861, Invitrogen) for 30 min at 37 °C in the dark, then measured using flow cytometry (BD FACS Calibur). C11-BODIPY (581/591) emission was measured using the FL1 channel. Meanwhile, the cells were seeded at 2.5×10^5 per well in a live cell imaging culture dish and incubated in 2 μM C11-BODIPY (581/591) and 200 nM MitoTracker Deep Red for 30 min at 37 °C in the dark, followed by observation using microscopy.

LPO Measurement by Liperfluo Probe. The lipid peroxidation level was analyzed by Liperfluo. Cells were seeded at 2.5×10^5 per well in a live cell imaging culture dish. After the indicated treatment, the cells were incubated in 2 μM Liperfluo (Cat. No. L248, Dojindo) and 200 nM MitoTracker Deep Red for 30 min at 37 °C in the dark, followed by observation using microscopy.

Mitochondrial Superoxide Measurement. The mitochondrial superoxide level was analyzed by MitoSOX Red, a mitochondrial superoxide indicator. Cells were harvested, incubated in PBS buffer containing 5 μM MitoSOX Red, and stained for 30 min at 37 °C in the dark, then measured using flow cytometry. MitoSOX Red emission was measured using the FL2 channel.

GSH and GSH/GSSG Measurement. GSH levels and the GSH/GSSG ratio were measured using a glutathione assay kit (Cat. No. S0052, Beyotime) according to the product instructions.

MDA Measurement. Cardiac MDA levels were measured using the thiobarbituric acid reactive substances (TBARS) assay kit (Cat. No. 10009055, Cayman Chemical) according to the product instructions.

Transmission Electron Microscopy (TEM). Myocardium was freshly isolated from the indicated mice and then cut into small pieces (1 mm × 1 mm × 1 mm) in 2.5% glutaraldehyde. The samples were fixed at 4 °C in 2.5% glutaraldehyde overnight and then postfixed, embedded, cut, and mounted into the Gatan holder for observation under a FEI Tecnai Spirit 120-kV TEM.

Echocardiography. Transthoracic echocardiography was performed on anesthetized mice to obtain two-dimensional targeted M-mode images on the short axis at the level of the papillary muscle using a Visual Sonics Vevo2100 μLtrasonography system. LVEF and LVFS were calculated by LV dimensions to quantify the degree of cardiac systolic and diastolic performance.

Histology. Heart tissues were rapidly isolated and fixed overnight with 4% paraformaldehyde; then they were embedded in paraffin and serially sectioned at 5-μm thickness. The sections were then incubated with anti-4-HNE (Cat. No. ab46545, Abcam) antibody overnight, followed by incubation with a secondary antibody for 30 min at room temperature. To measure the collagen fibrosis in myocardium, selected sections were stained with Masson's Trichrome Staining Kit (Cat. No. G1345, Solarbio). Images were captured by a Leica Aperio VESA8 Digital Pathology Scanner.

Blue Native Electrophoresis. To analyze the dimeric and monomeric forms of SLC25A11, MEF cells and cardiac tissues were collected and mitochondria fractions of these were isolated and then lysed in lysis buffer (50 mM Tris·HCl [pH 7.4], 150 mM NaCl, and 0.5% Nonidet P-40, protease inhibitor mixture). Lysates with the presence or absence of SDS were separated by native PAGE, blotted to nitrocellulose membranes and incubated with the indicated antibodies.

TAP/MS. HeLa cells transfected with vector and FUNDC2-SBP-2*Flag plasmid were collected and lysed in lysis buffer to obtain tissue or cell lysates. Lysates were added to anti-Flag M2 agarose beads (Cat. No. M8823, Sigma) overnight at 4 °C. Then the beads were washed to remove the remaining trapped lysis buffer, followed by the addition of tobacco etch virus (TEV) protease (Cat. No. 12575, Invitrogen) to cleave the proteins from the Flag-tags. After centrifugation, the eluents were collected, combined, and incubated with streptavidin sepharose (Cat. No. 17-5113-01, GE Healthcare) at 4 °C for 3 h. Afterward, the samples were centrifuged and the precipitates were separated by SDS-PAGE and silver stain analysis. All the distinctive bands that could be observed were collected for analysis by mass spectrometry.

Statistical Analysis. Data are shown as the mean ± SEM. Statistical analysis was performed by two-tailed Student's *t* test or one-way ANOVA with Tukey's post hoc test. ns, nonsignificant; $*P < 0.05$; $**P < 0.01$; $***P < 0.001$.

Data Availability. All study data are included in the article and/or *SI Appendix*.

ACKNOWLEDGMENTS. We thank Tong Zhao at the Institute of Microbiology (Chinese Academy of Sciences [CAS]), Yao Song at Peking University Health Science Center, and Zhongshuang Lv and Xueke Tan at the Institute of Biophysics (CAS) for their technical support with flow cytometry, echocardiography, and TEM sample preparation, respectively. We thank Professor Moshi Song at the Institute of Zoology (CAS) for providing the H9c2 cells. We also thank Professor Mark Bartlam and Professor Xudong Liao for their English language editing of the manuscript. This research was supported by the grants 91849201 and 31790404 from the National Natural Science Foundation of China and Grant 2019YFA0508601 from the Ministry of Science and Technology of China (to Q.C.); Grant 2020YFA0803702 from the Ministry of Science and Technology of China and Grant 91854105 from the National Natural Science Foundation of China (to L.L.); and Grant 31970716 from the National Natural Science Foundation of China (to Y.L.).

Author affiliations: [a]State Key Laboratory of Membrane Biology, Institute of Zoology, Chinese Academy of Sciences, Beijing, 100101, China; [b]University of Chinese Academy of Sciences, Beijing, 100049, China; [c]Beijing Institute for Stem Cell and Regenerative Medicine, Beijing, 100101, China; [d]State Key Laboratory of Agricultural Microbiology, College of Veterinary Medicine, Huazhong Agricultural University, Wuhan, 430070, China; and [e]Interdisciplinary Center of Cell Response, State Key Laboratory of Medicinal Chemical Biology, College of Life Sciences, Nankai University, Tianjin, 300071, China

1. S. J. Dixon *et al.*, Ferroptosis: An iron-dependent form of nonapoptotic cell death. *Cell* **149**, 1060–1072 (2012).
2. W. S. Yang *et al.*, Regulation of ferroptotic cancer cell death by GPX4. *Cell* **156**, 317–331 (2014).
3. C. Mao *et al.*, DHODH-mediated ferroptosis defence is a targetable vulnerability in cancer. *Nature* **593**, 586–590 (2021).
4. C. C. Ding *et al.*, MESH1 is a cytosolic NADPH phosphatase that regulates ferroptosis. *Nat. Metab.* **2**, 270–277 (2020).
5. B. Chu *et al.*, ALOX12 is required for p53-mediated tumour suppression through a distinct ferroptosis pathway. *Nat. Cell Biol.* **21**, 579–591 (2019).
6. S. Doll *et al.*, FSP1 is a glutathione-independent ferroptosis suppressor. *Nature* **575**, 693–698 (2019).
7. S. E. Wenzel *et al.*, PEBP1 Wardens Ferroptosis by Enabling Lipoxygenase Generation of Lipid Death Signals. *Cell* **171**, 628–641.e26 (2017).
8. M. Hayano, W. S. Yang, C. K. Corn, N. C. Pagano, B. R. Stockwell, Loss of cysteinyl-tRNA synthetase (CARS) induces the transsulfuration pathway and inhibits ferroptosis induced by cystine deprivation. *Cell Death Differ.* **23**, 270–278 (2016).
9. X. Sun *et al.*, HSPB1 as a novel regulator of ferroptotic cancer cell death. *Oncogene* **34**, 5617–5625 (2015).
10. B. R. Stockwell *et al.*, Ferroptosis: A regulated cell death nexus linking metabolism, redox biology, and disease. *Cell* **171**, 273–285 (2017).
11. J. Y. Lee *et al.*, Polyunsaturated fatty acid biosynthesis pathway determines ferroptosis sensitivity in gastric cancer. *Proc. Natl. Acad. Sci. U.S.A.* **117**, 32433–32442 (2020).
12. K. Bersuker *et al.*, The CoQ oxidoreductase FSP1 acts parallel to GPX4 to inhibit ferroptosis. *Nature* **575**, 688–692 (2019).
13. T. Tadokoro *et al.*, Mitochondria-dependent ferroptosis plays a pivotal role in doxorubicin cardiotoxicity. *JCI Insight* **5**, 132747 (2020).
14. X. Fang *et al.*, Loss of cardiac ferritin H facilitates cardiomyopathy via Slc7a11-mediated ferroptosis. *Circ. Res.* **127**, 486–501 (2020).
15. X. Fang *et al.*, Ferroptosis as a target for protection against cardiomyopathy. *Proc. Natl. Acad. Sci. U.S.A.* **116**, 2672–2680 (2019).
16. J. P. Friedmann Angeli *et al.*, Inactivation of the ferroptosis regulator Gpx4 triggers acute renal failure in mice. *Nat. Cell Biol.* **16**, 1180–1191 (2014).

17. N. Yamada *et al.*, Ferroptosis driven by radical oxidation of n-6 polyunsaturated fatty acids mediates acetaminophen-induced acute liver failure. *Cell Death Dis.* **11**, 144 (2020).
18. J. R. Friedman, J. Nunnari, Mitochondrial form and function. *Nature* **505**, 335–343 (2014).
19. Z. Cheng, M. Ristow, Mitochondria and metabolic homeostasis. *Antioxid. Redox Signal.* **19**, 240–242 (2013).
20. R. B. Hamanaka, N. S. Chandel, Mitochondrial reactive oxygen species regulate cellular signaling and dictate biological outcomes. *Trends Biochem. Sci.* **35**, 505–513 (2010).
21. C. Perricone, C. De Carolis, R. Perricone, Glutathione: A key player in autoimmunity. *Autoimmun. Rev.* **8**, 697–701 (2009).
22. O. W. Griffith, A. Meister, Origin and turnover of mitochondrial glutathione. *Proc. Natl. Acad. Sci. U.S.A.* **82**, 4668–4672 (1985).
23. L. H. Lash, T. M. Visarius, J. M. Sall, W. Qian, J. J. Tokarz, Cellular and subcellular heterogeneity of glutathione metabolism and transport in rat kidney cells. *Toxicology* **130**, 1–15 (1998).
24. Z. Chen, L. H. Lash, Evidence for mitochondrial uptake of glutathione by dicarboxylate and 2-oxoglutarate carriers. *J. Pharmacol. Exp. Ther.* **285**, 608–618 (1998).
25. B. S. Cummings, R. Angeles, R. B. McCauley, L. H. Lash, Role of voltage-dependent anion channels in glutathione transport into yeast mitochondria. *Biochem. Biophys. Res. Commun.* **276**, 940–944 (2000).
26. F. Xu, D. A. Putt, L. H. Matherly, L. H. Lash, Modulation of expression of rat mitochondrial 2-oxoglutarate carrier in NRK-52E cells alters mitochondrial transport and accumulation of glutathione and susceptibility to chemically induced apoptosis. *J. Pharmacol. Exp. Ther.* **316**, 1175–1186 (2006).
27. L. M. Booty *et al.*, Selective disruption of mitochondrial thiol redox state in cells and in vivo. *Cell Chem. Biol.* **26**, 449–461.e8 (2019).
28. C. Kumar *et al.*, Glutathione revisited: A vital function in iron metabolism and ancillary role in thiol-redox control. *EMBO J.* **30**, 2044–2056 (2011).
29. G. Calabrese, B. Morgan, J. Riemer, Mitochondrial glutathione: Regulation and functions. *Antioxid. Redox Signal.* **27**, 1162–1177 (2017).
30. S. C. Lu, Regulation of glutathione synthesis. *Mol. Aspects Med.* **30**, 42–59 (2009).
31. L. J. Yant *et al.*, The selenoprotein GPX4 is essential for mouse development and protects from radiation and oxidative damage insults. *Free Radic. Biol. Med.* **34**, 496–502 (2003).
32. H. Zhong, H. Yin, Role of lipid peroxidation derived 4-hydroxynonenal (4-HNE) in cancer: Focusing on mitochondria. *Redox Biol.* **4**, 193–199 (2015).
33. W. S. Yang, B. R. Stockwell, Ferroptosis: Death by lipid peroxidation. *Trends Cell Biol.* **26**, 165–176 (2016).
34. M. Gao *et al.*, Role of mitochondria in ferroptosis. *Mol. Cell* **73**, 354–363.e3 (2019).
35. P. K. Singal, N. Iliskovic, Doxorubicin-induced cardiomyopathy. *N. Engl. J. Med.* **339**, 900–905 (1998).
36. K. F. Cho *et al.*, Split-TurboID enables contact-dependent proximity labeling in cells. *Proc. Natl. Acad. Sci. U.S.A.* **117**, 12143–12154 (2020).
37. K. J. De Vos *et al.*, VAPB interacts with the mitochondrial protein PTPIP51 to regulate calcium homeostasis. *Hum. Mol. Genet.* **21**, 1299–1311 (2012).
38. S. Kawano *et al.*, Structure-function insights into direct lipid transfer between membranes by Mmm1-Mdm12 of ERMES. *J. Cell Biol.* **217**, 959–974 (2018).
39. Z. Chen, D. A. Putt, L. H. Lash, Enrichment and functional reconstitution of glutathione transport activity from rabbit kidney mitochondria: Further evidence for the role of the dicarboxylate and 2-oxoglutarate carriers in mitochondrial glutathione transport. *Arch. Biochem. Biophys.* **373**, 193–202 (2000).
40. J. Garcia *et al.*, Regulation of mitochondrial glutathione redox status and protein glutathionylation by respiratory substrates. *J. Biol. Chem.* **285**, 39646–39654 (2010).
41. E. W. Trotter, C. M. Grant, Overlapping roles of the cytoplasmic and mitochondrial redox regulatory systems in the yeast Saccharomyces cerevisiae. *Eukaryot. Cell* **4**, 392–400 (2005).
42. S. M. Swain, F. S. Whaley, M. S. Ewer, Congestive heart failure in patients treated with doxorubicin: A retrospective analysis of three trials. *Cancer* **97**, 2869–2879 (2003).
43. M. Ueno *et al.*, Doxorubicin induces apoptosis by activation of caspase-3 in cultured cardiomyocytes in vitro and rat cardiac ventricles in vivo. *J. Pharmacol. Sci.* **101**, 151–158 (2006).
44. F. S. Carvalho *et al.*, Doxorubicin-induced cardiotoxicity: From bioenergetic failure and cell death to cardiomyopathy. *Med. Res. Rev.* **34**, 106–135 (2014).
45. A. R. Coelho *et al.*, Berberine-induced cardioprotection and Sirt3 modulation in doxorubicin-treated H9c2 cardiomyoblasts. *Biochim. Biophys. Acta Mol. Basis Dis.* **1863**, 2904–2923 (2017).
46. Z. M. Xu, C. B. Li, Q. L. Liu, P. Li, H. Yang, Ginsenoside Rg1 prevents doxorubicin-induced cardiotoxicity through the inhibition of autophagy and endoplasmic reticulum stress in mice. *Int. J. Mol. Sci.* **19**, E3658 (2018).
47. J. Yin *et al.*, Doxorubicin-induced mitophagy and mitochondrial damage is associated with dysregulation of the PINK1/parkin pathway. *Toxicol. In Vitro* **51**, 1–10 (2018).
48. T. R. Mancilla, L. R. Davis, G. J. Aune, Doxorubicin-induced p53 interferes with mitophagy in cardiac fibroblasts. *PLoS One* **15**, e0238856 (2020).
49. K. B. Wallace, V. A. Sardão, P. J. Oliveira, Mitochondrial determinants of doxorubicin-induced cardiomyopathy. *Circ. Res.* **126**, 926–941 (2020).
50. S. Cardoso *et al.*, Doxorubicin increases the susceptibility of brain mitochondria to Ca(2+)-induced permeability transition and oxidative damage. *Free Radic. Biol. Med.* **45**, 1395–1402 (2008).
51. Q. Ma *et al.*, Mitochondrial PIP3-binding protein FUNDC2 supports platelet survival via AKT signaling pathway. *Cell Death Differ.* **26**, 321–331 (2019).